Green Chemistry

ROYAL SOCIETY OF CHEMISTRY

PAPER

**Cite this:** *Green Chem.*, 2025, **27**, 4196

# Disclosing multiple factors influencing enantioselective copolymerization of $CO_2$ with *meso*-epoxides using β-diiminate Zn catalysts†

Yolanda Rusconi,[a,b] Massimo Christian D'Alterio,[b] Claudio De Rosa,[b] Geoffrey W. Coates[c] and Giovanni Talarico *[a,b]

The enantioselective ring-opening copolymerization (ROCOP) of cyclohexene oxide (CHO) and carbon dioxide ($CO_2$) to produce isotactic poly(cyclohexene carbonate) (iPCHC) was systematically investigated using chiral $C_1$-symmetric zinc β-diiminate (BDI) catalysts. A combination of density functional theory (DFT), molecular steric descriptors (%$V_{Bur}$), and the activation strain model (ASM) was employed to elucidate the mechanistic pathways and factors governing enantioselectivity. We found that chiral monomeric BDI catalysts exhibit intrinsic enantioselective properties in *meso*-desymmetrization polymerization catalysis, which are significantly enhanced upon formation of dimeric complexes with *anti* and *syn* conformations. The predicted enantioselectivity, arising during the CHO ring-opening step, explains the experimental combination of selected stereocenters on the ligand and preferred stereochemistry of the polymer chain. This study identifies key factors influencing ROCOP enantioselectivity, including monomer deformation, ligand steric effects dictated by the number of chiral centers, and noncovalent interactions, all contributing additively to the observed selectivity. These insights provide a better understanding of the mechanistic origins of enantioselectivity in CHO/$CO_2$ ROCOP and offer guidance for the design of more efficient catalysts.

Received 28th January 2025,
Accepted 6th March 2025

DOI: 10.1039/d5gc00523j

rsc.li/greenchem

### Green foundation

1. The copolymerization of carbon dioxide ($CO_2$) and *meso*-epoxides is a promising strategy for utilizing $CO_2$ as a renewable feedstock, enabling the synthesis of polymeric materials with functional and desirable properties.
2. Enantioselective ring-opening copolymerization (ROCOP) of $CO_2$ and *meso*-epoxides yields isotactic polycarbonates (iPCs), which are potentially biodegradable and recyclable. These materials offer an eco-friendly alternative to conventional fossil-fuel-based plastics, contributing to the circular economy. This study delves into the critical factors influencing ROCOP enantioselectivity, including monomer deformation, ligand steric effects modulated by the number and arrangement of chiral centers and noncovalent interactions.
3. A deeper understanding of these selectivity factors could pave the way for designing more efficient catalysts replacing conventional plastics and promoting the utilization of alternative feedstocks. Ultimately, this advances carbon recirculation by transforming $CO_2$ from a waste product into a valuable resource.

## Introduction

The use of carbon dioxide ($CO_2$) to produce commodities has been deeply investigated in recent years. $CO_2$ is an ideal feedstock because it is nontoxic, inexpensive, abundant on Earth and its consumption could contribute to the mitigation of the global temperature rise.[1] The copolymerization of $CO_2$ and *meso*-epoxides[2,3] represents a viable route since it leads to the formation of polycarbonates (PCs) that are potentially biodegradable and recyclable materials. The inclusion of cyclohexene oxide (CHO) in the polymer backbone overcomes one of the problems associated with most aliphatic polycarbonates such as their low glass transition temperature ($T_g$) values; indeed, the $T_g$ of poly(cyclohexene carbonate) (PCHC) can reach up to 120 °C and it has tensile modulus ~3.6 GPa, enabling its use as engineering plastic.[4,5] Furthermore, PCHC is chemically recyclable to epoxide and carbon dioxide by using homo- and heterodinuclear catalysts highly active in solid-state depolymerizations.[6–8]

---

[a] *Scuola Superiore Meridionale, Largo San Marcellino, 80138 Napoli, Italy. E-mail: talarico@unina.it*

[b] *Dipartimento di Scienze Chimiche, Università degli Studi di Napoli Federico II, 80126 Napoli, Italy*

[c] *Department of Chemistry and Chemical Biology, Baker Laboratory, Cornell University, Ithaca, NY 14853-1301, USA*

† Electronic supplementary information (ESI) available. See DOI: **https://doi.org/10.1039/d5gc00523j**

The enantioselective copolymerization of $CO_2$ and CHO *via* ring-opening copolymerization (ROCOP)[9–13] produces isotactic poly(cyclohexene carbonate) (*i*PCHC), a semicrystalline thermoplastic with physical properties highly dependent on its stereoregularity.[4] Being that CHO is a *meso*-compound displaying two neighboring stereocenters in opposite configurations, the selective ring-opening at one of the two chiral carbons results in the desymmetrization of this monomer and formation of two different repeating units. The attack at *S*- or *R*-configured carbons produces an *R*,*R*- or *S*,*S*-chain, respectively (Scheme 1a).

*Meso*-desymmetrization catalysis is a valuable synthetic approach when selective activation of one stereogenic center is achieved during the catalytic cycle.[14,15] Notable examples include the stereoselective ring-opening polymerization (ROP) of *meso*-lactide (*meso*-LA) by chiral aluminum complexes (Scheme 1b). In this process, preferential attack at the carbonyl group adjacent to the *R* or *S* stereogenic center, determined by catalyst chirality, results in the formation of highly syndiotactic poly(lactic acid) (*s*PLA).[16–18] DFT calculations have rationalized this preference,[19] attributing it to repulsive interactions between the ligand and the monomer, which also explain the stereoselective ROP of racemic lactide (*rac*-LA),[20] and the regioselective ROP of 3-methyl glycolide.[21]

Coates and coworkers reported a series of $C_1$-symmetric zinc β-diiminate catalysts (**BDI**, Scheme 2) that displayed high activity, carbon linkages and a noteworthy enantioselectivity towards the ROCOP of $CO_2$ and *meso*-CHO.[12] The BDI family having 2,6-dimethylphenyl as an *N*-aryl group have been classified as first ($G_1$) and second ($G_2$) generations depending on the number of chiral centers and size of the chiral substituents (see the single *S* stereocenter for $G_1$ and the two *S* stereocenters for $G_2$ in Scheme 2). Interestingly, moving from $G_1$ to $G_2$ systems, the amplification of the enantioselectivity in the copolymerization of CHO and $CO_2$ has been obtained.[12d]

Mechanistic studies suggested that, starting from monomeric species (**BDI-M**, Scheme 3a), the $CO_2$/CHO copolymerization catalyzed by **BDI** systems involves dimeric species (**BDI-D**) that can adopt *anti* (**BDI-D*anti***, Scheme 3b) or *syn* (**BDI-D*syn***, Scheme 3c) conformations.[12] Indeed, X-ray analysis of the catalytic precursor revealed its preferred dimeric structures, with a core consisting of a 6-membered ring containing the two Zn centers, one acetate bridging with both its oxygens in a $k^2\mu$ fashion while the other in a $k^1\mu$ fashion. The **BDI1** complex (Scheme 2) exhibited an *anti*-conformation (**BDI1-D*anti***, Scheme 3b), bearing the *N*-aryl and the *sec*-phenethyl groups on opposite sides of the plane formed by the Zn atoms and the acetate groups.[12] The *syn*-conformation (**BDI1-D*syn***, Scheme 3c), bearing the substituents on the same side of the plane, was not observed. We were intrigued by the asymmetric amplification going from $G_1$ to $G_2$ generations that are among the most stereoselective reported in the literature.[22] At the same time, our initial guess was that chiral **BDI-M** may also show an intrinsic enantioselective character into the *meso*-desymmetrization catalysis further amplified by the formation of dimeric species, considered as the active species in solution.[12c] To assess this hypothesis, we used computational methods rooted in density functional theory (DFT), performing an extensive mechanistic study on the initiation and propagation steps of the $CO_2$/CHO ROCOP and thorough understanding of the factors affecting the enantioselective copolymerization. The DFT results were combined with a steric molecular descriptor (%$V_{\text{Bur}}$)[23,24] and the application of activation strain model (ASM)[25,26] analysis to better identify the origin of the enantioselective ROCOP promoted by both **BDI-M** and **BDI-D** species. In the following, we selected **BDI1** (Scheme 2) as a prototypical example of the $G_1$ generation[12d] and we will discuss in the first part the results computed on **BDI1-M** and then in the second part on **BDI1-D**. Finally, we will extend the calculations to the **BDI5** catalyst of the $G_2$ generation (Scheme 2) to check the reliability of our computations with respect to the experimental trend[12d] and to compare our data with recent reports in the literature.[27]

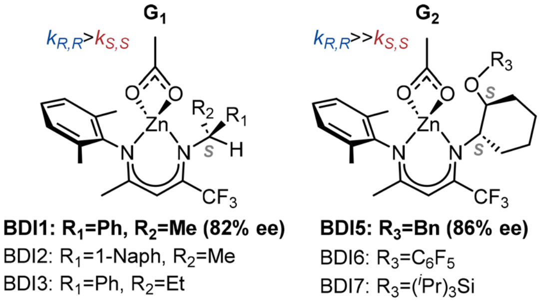

Scheme 2 Structures of $G_1$ and $G_2$ generations of zinc β-diiminate catalysts for enantioselective ROCOP of CHO and $CO_2$.[12d]

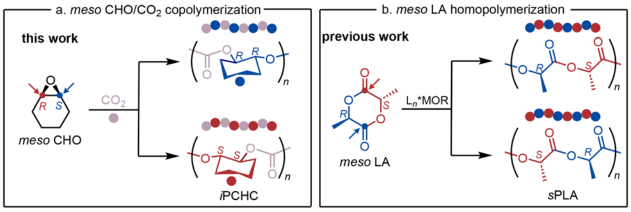

Scheme 1 *Meso*-desymmetrization catalysis in the ROCOP of CHO and $CO_2$ (a) and in the ROP of *meso*-LA (b).

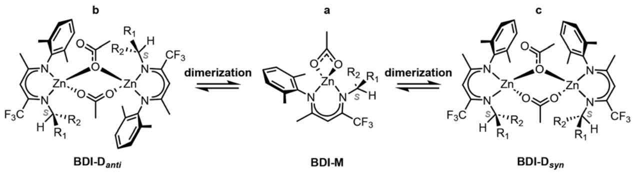

Scheme 3 Schematic equilibrium of BDI systems with monomeric (**BDI-M**, a), and dimeric (**BDI-D**) species with *anti* (**BDI-D*anti***, b) and *syn* (**BDI-D*syn***, c) conformations.

## Computational methods

All DFT calculations and geometry optimizations were performed using the Gaussian16 set of programs,[28] using the B3LYP functional.[29] The electronic configuration has been described using two different layers of basis set: SDD for Zn and SVP for all the atoms[30] for characterization of the stationary points using vibrational analysis, and this analysis has also been used to calculate zero-point energies and thermal (enthalpy and entropy) corrections (298.15 K, 1 bar). Improved electronic energies have been obtained from single-point energy calculations using the SDD basis set for Zn and 6-311G (d,p) basis set for all the atoms, with a solvation contribution (PCM model,[31] toluene) and dispersion corrections (D3BJ).[32] These energies added to the SVP-level thermal corrections are named $\Delta G$ in the text. Calculations including D3BJ in geometry optimization as well as different computational approaches have been performed to assess the discrepancies of computational results and for comparison with the literature (Table S1†). The counterpoise corrections of the basis set superposition error (BSSE)[33] have been calculated with the same basis sets used for the energy refining, specifying the number of fragments composing the structure of interest. When we extended our analysis to **BDI5-D** ($G_2$ generation), we selected the computational approach used by Cramer[27] (ωB97XD(SMD)/SDD/6-311G+(d,p)//B3LYP-D3BJ/LANL2DZ/6-31G(d))[34] for the initiation reaction whereas for the propagation steps we fully optimized the chiral chains (ESI, Scheme S1†). Details of entropic corrections,[35] ASM, %$V_{\mathrm{Bur}}$ and noncovalent interaction analysis (NCI)[36] and visualization are also reported in the ESI.†

## Results and discussion

### *Meso*-desymmetrization ROCOP by monomeric BDI1 species

The Gibbs energetic profiles for $CO_2$/CHO ROCOP initiation and propagation steps promoted by **BDI1-M** are summarized in Fig. 1. The catalytic cycle begins with the coordination of CHO to the Zn center, forming intermediate **INT1-M**. This is followed by the epoxide ring-opening, driven by the nucleophilic attack of the carbonyl oxygen of the acetate on the electrophilic carbon of the CHO epoxide. The enantioselectivity of the initiation reaction is determined by the Gibbs energetic difference ($\Delta\Delta G_{enantio}$) between the attack on *S* and *R* carbon atoms of CHO as illustrated by **TS1-M*R*,*R*** and **TS1-M*S*,*S*** (depicted with blue and red lines in Fig. 1).

Once the ring is opened, intermediate **INT2-M** is formed. This is followed by an attack of the epoxide oxygen on the electrophilic carbon of $CO_2$ *via* **TS2-M**, yielding the thermodynamically stable intermediate **INT3-M** with a growing polymer chain. The ring-opening of CHO serves as both the rate-determining step (RDS) and enantioselectivity-determining step, while $CO_2$ insertion proceeds rapidly. After coordination of a second CHO molecule (**INT1′-M**), the growing chain ($(OR)CO_2^-$) is able to selectively attack the latter (**TS1′-**

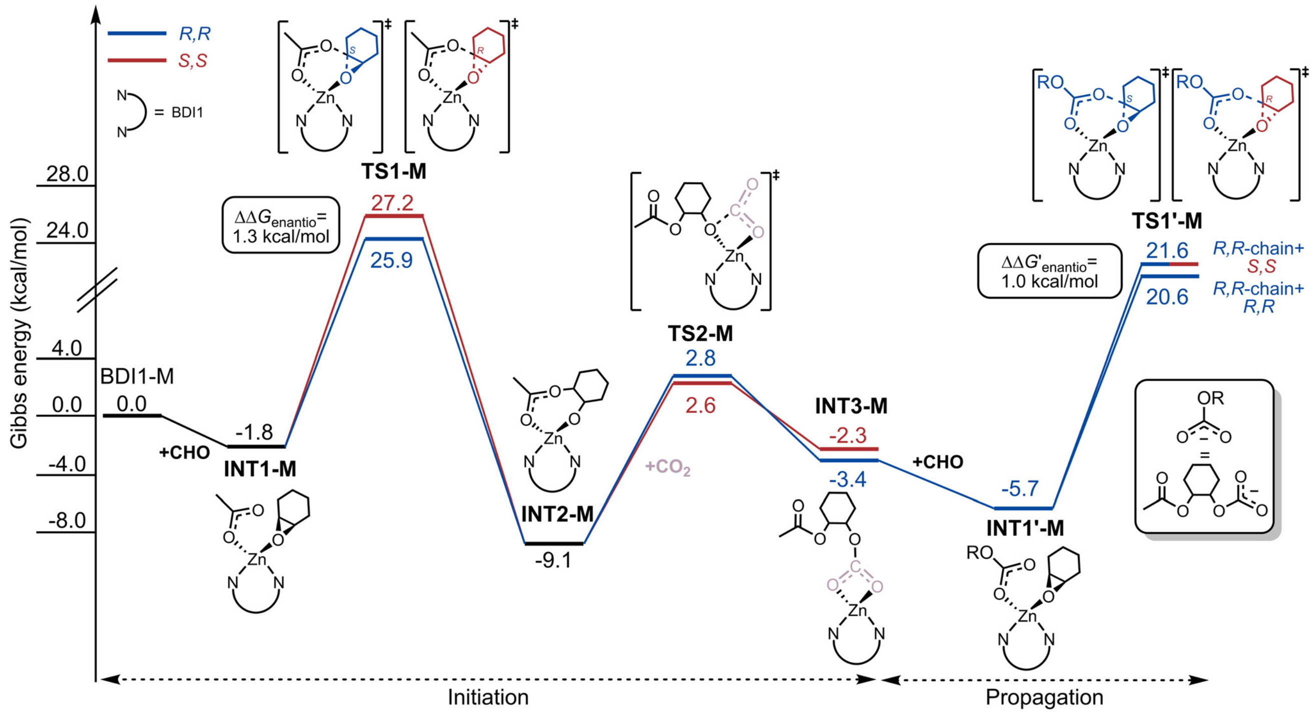

**Fig. 1** Gibbs energy profile for initiation and propagation steps in the CHO/$CO_2$ copolymerization catalyzed by **BDI1-M**. The blue and red pathways correspond to the formation of *R*,*R*- and *S*,*S*-configured chains based on attacks on the *S* and *R* carbons of CHO, respectively. The presence of an entire growing unit ($(OR)CO_2^-$) is simulated in the propagation.

**M**$_{R,R}$ and **TS1′-M**$_{S,S}$). DFT calculations predict the preferential formation of *R*,*R*-configured repeat units during both initiation and propagation, with $\Delta\Delta G_{enantio}$ and $\Delta\Delta G'_{enantio}$ values of 1.3 kcal mol$^{-1}$ and 1.0 kcal mol$^{-1}$, respectively (Fig. 1). These results are in line with experimental findings, supporting our initial hypothesis that chiral monomeric Zn(BDI) species exhibit inherent enantioselectivity in *meso*-desymmetrization catalysis. However, the calculated enantioselectivities are lower than those observed experimentally during the ROCOP of $CO_2$ and CHO.

To further explore the influence of chain chirality, we modeled also the propagation step with the *S*,*S*-configured unit as growing chain. DFT results (Fig. S1†) confirm the modest enantioselectivity imparted by **BDI1-M**, regardless of the chirality of the last inserted unit.

To clarify the origin of **BD1-M** enantioselectivity, we employed the ASM analysis[25] combined with the steric maps of % buried volume analysis (%$V_{\text{Bur}}$).[23] ASM quantifies the strain energy ($\Delta E_{\text{Strain}}$) required to deform the two interacting fragments – the catalyst precursor and growing chain ($\Delta E_{\text{Strain(Cat+chain)}}$) and the monomer ($\Delta E_{\text{Strain(Mon)}}$) – from their optimal geometries into the conformations required for the reaction. We successfully applied such a combined approach for understanding the origin of transition metal-catalyzed stereoselective α-olefin polymerization[37] as well as the ROP of *rac*-LA.[38] The fragmentation approach used for the ROCOP is illustrated in Fig. S2† and detailed methodologies are provided in the ESI.†

The $\Delta\Delta E_{\text{Strain}}$ values (Table 1) for the two competing attack pathways on CHO indicate that the primary contributor to enantioselectivity is the monomer deformation energy ($\Delta E_{\text{Strain(Mon)}}$). The latter favors attack on the *S* carbon of CHO over the *R* carbon during both the initiation (**TS1-M**$_{R,R}$ and **TS1-M**$_{S,S}$) and propagation (**TS1′-M**$_{R,R}$ and **TS1′-M**$_{S,S}$) steps.

The inherent structural differences in the deformation energy required for the *S* and *R* pathways appear to be the main driver of the observed enantioselectivity of **BDI1-M**. A detailed examination of the competitive TS structures (Fig. 2) using a modified %$V_{\text{Bur}}$ analysis,[23,24] specifically designed to visualize octant occupancies (Fig. S3†), provides further insight into the origins of **BDI1-M** enantioselectivity.

Table 1 ASM results for selected TSs leading to the enantioselectivity of the initiation and propagation steps for ROCOP of $CO_2$ and CHO promoted by **BDI1-M**

| Initiation | **TS1-M**$_{R,R}$ | **TS1-M**$_{S,S}$ | $\Delta\Delta E^a$ |
|---|---|---|---|
| $\Delta E_{\text{Strain}}$ | 64.4 | 70.4 | 6.0 |
| $\Delta E_{\text{Strain(Cat+chain)}}$ | 32.9 | 32.0 | −1.0 |
| $\Delta E_{\text{Strain(Mon)}}$ | 31.4 | 38.4 | **7.0** |
| **Propagation** | **TS1′-M**$_{R,R}$ | **TS1′-M**$_{S,S}$ | $\Delta\Delta E^a$ |
| $\Delta E_{\text{Strain}}$ | 67.6 | 74.4 | 6.7 |
| $\Delta E_{\text{Strain(Cat+chain)}}$ | 35.0 | 32.5 | −2.5 |
| $\Delta E_{\text{Strain(Mon)}}$ | 32.6 | 41.8 | **9.2** |

[a] $\Delta\Delta E$ values (kcal mol$^{-1}$) calculated as the difference between each $\Delta E$ term for **TS1-M** leading to an *S*,*S*-chain and *R*,*R*-chain.

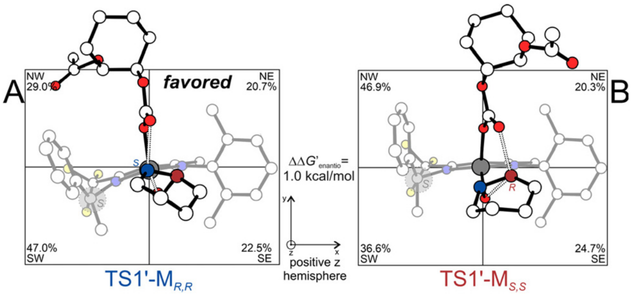

Fig. 2 DFT-optimized geometries for **TS1′-M** with the attack on *S* (A) and *R* (B) CHO stereocenters with the steric maps calculated by %$V_{\text{Bur}}$ for the propagation step promoted by **BDI1-M** with *R*,*R*-configured repeat units.

In the pathway involving attack on the *S* carbon of CHO, the monomer preferentially occupies the unencumbered southeast (SE) octants (Fig. 2A). This orientation maintains a larger distance (4.6 Å) between the monomer and the chiral carbon of the *N*-aryl imines in the ligand. Conversely, the attack on the *R* carbon of CHO results in a closer proximity (4.4 Å) between these two atoms, as shown in Fig. 2B.

This closer interaction forces part of the ligand to tilt, resulting in the occupation of the more congested southwest (SW) and northwest (NW) quadrants.

We can argue that this effect is mainly due to the interaction between the chirality of the ligand and the stereogenic centers of the monomer whereas the chirality of the growing chain plays a limited effect. Indeed, this feature is similar for initiation and propagation steps and the ASM results (Table 1) combined with the %$V_{\text{Bur}}$ steric maps (Fig. 2 and Fig. S4†) support this interpretation.

### *Meso*-desymmetrization ROCOP by dimeric BDI1 species

After unveiling the enantioselective features of **BDI1-M**, we investigated the initiation and propagation cycles for the catalytic species in its dimeric form (**BDI1-D**). Several mechanistic studies have suggested that the dimeric forms act as the active species in this reaction, as they are considered kinetically more feasible.[12,39,40]

We calculated, initially, the Gibbs energies for the formation of the *anti* and *syn* dimeric species (**BDI1-D**$_{anti}$ and **BDI1-D**$_{syn}$) corrected by BSSE ($\Delta G_{\text{dim}}$). The **BDI1-D**$_{anti}$ ($\Delta G_{\text{dim}}$ = −11.0 kcal mol$^{-1}$) is more stable than **BDI1-D**$_{syn}$ ($\Delta G_{\text{dim}}$ = −5.9 kcal mol$^{-1}$) by around 5 kcal mol$^{-1}$ (Fig. S5†). This finding is consistent with prior X-ray structural data of the catalyst[12d] and earlier calculations on zinc pyridylamido ligands.[40]

The reaction pathways for the initiation step of ROCOP of CHO and $CO_2$ catalyzed by **BDI1-D**$_{anti}$ (solid line) and **BDI1-D**$_{syn}$ (dashed line) are presented in Fig. 3 (separate profiles in Fig. S6 and S7†).

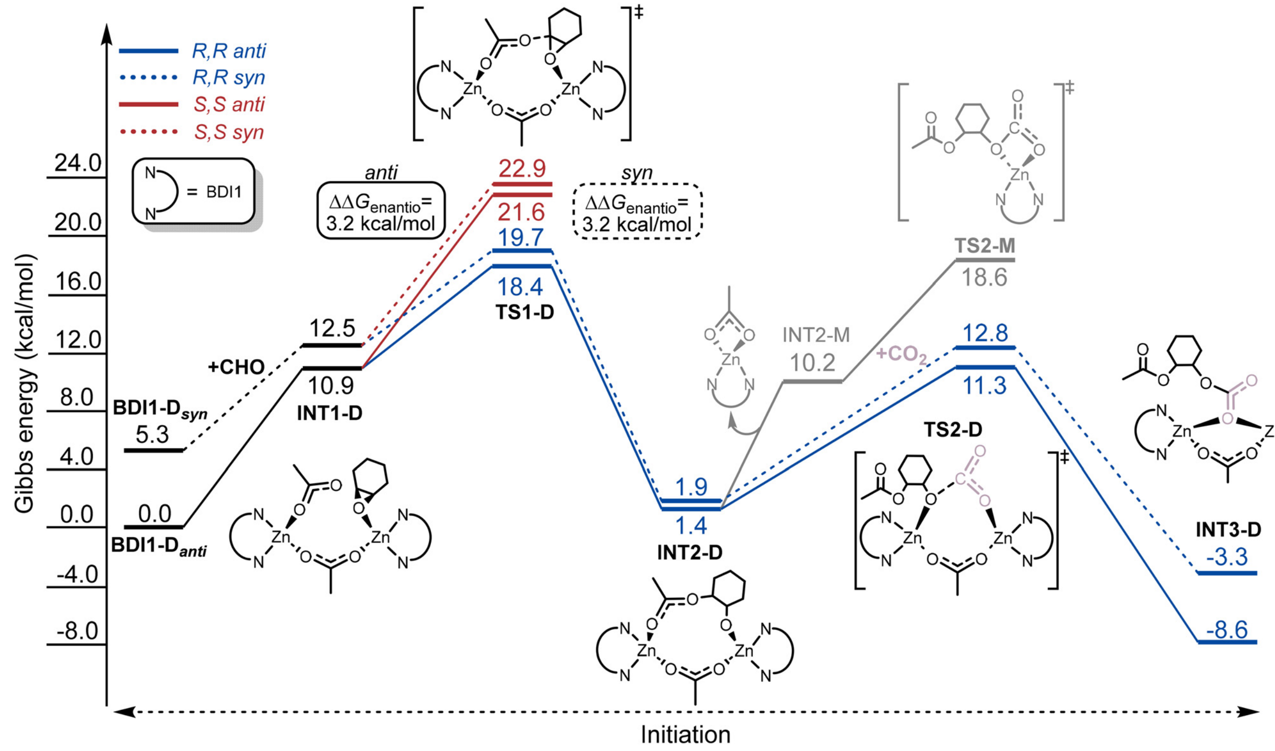

**Fig. 3** Gibbs energy profile of the initiation reaction for CHO and $CO_2$ ROCOP involving **BDI1-D*anti*** (full line), **BDI1-D*syn*** (dashed line) and **BDI1-M** (in grey) species. Energies (kcal $mol^{-1}$) are calculated with respect to the most stable **BDI1-D*anti*** species. The paths leading to the formation of the *R*,*R*-chain and *S*,*S*-chain are reported in blue and red, respectively.

Gibbs energies are referenced to the most stable species, **BDI1-D*anti*** + CHO (adding $CO_2$ after **INT2-D**). The catalytic attack by the carbonyl oxygen of acetate on the *S* stereocenter of CHO, following coordination, is energetically favored, resulting in the formation of an *R*,*R*-chain, consistent with experimental observations.[12] Although the activation energies for **BDI1-D*anti*** and **BDI1-D*syn*** are comparable when referenced to the most stable precursor (**BDI1-D*anti*** + CHO), **BDI1-D*syn*** exhibits lower activation energies when considered against its suitable reference point (Fig. 3). After we computed direct $CO_2$ insertion on the dimeric species, we also hypothesized the dissociation of a catalyst unit with formation of the monomeric **INT2-M** and following $CO_2$ insertion (**TS2-M**), as hypothesized experimentally and computationally (Fig. 3, grey color).[12d,27] However, the greater stability of the dimeric species results also in lower barriers for $CO_2$ insertion (compare **TS2-D** with **TS2-M** in Fig. 3). This agrees with experimental evidence that **BDI1** forms a tightly bound dimer, in contrast to the more labile **BDI5** complex[12d] and the higher dissociation energy of **BDI1-D** contributes to the elevated energy of **INT2-M** (10.2 kcal $mol^{-1}$). In any case, *both* **BDI1-D*anti*** and **BDI1-D*syn*** exhibit enantioselectivity during the initiation step, leading to the formation of *R*,*R*-chains as observed experimentally. Furthermore, both dimers amplify enantioselectivity compared to the monomeric species (Fig. 3 *vs.* Fig. 1), underscoring the role of dimerization in the amplification of the enantioselectivity.

The ASM analysis reported in Table 2 confirms the pivotal role played by the monomer deformation ($\Delta E_{\text{Strain(Mon)}}$) in destabilizing the attack at the *R*-configured carbon (**TS1-D*S,S*** *vs.* **TS1-D*R,R***). Indeed, the $\Delta\Delta E_{\text{Strain(Mon)}}$ difference is the main feature responsible for the enantioselectivity of the initiation step promoted by both **BDI1-D*anti*** and **BDI1-D*syn*** (values in bold in Table 2, 4.6 and 4.7 kcal $mol^{-1}$, respectively).

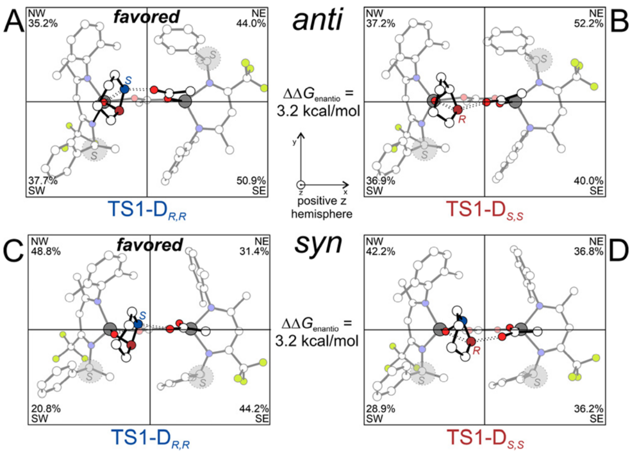

**Fig. 4** DFT geometries and $\%V_{\text{Bur}}$ (octants) of the RDS of **BDI1-D*anti*** (A and B) and **BDI1-D*syn*** (C and D) species for the initiation of the ROCOP of $CO_2$ and CHO.

Table 2 ASM results for selected TSs leading to the enantioselectivity of the initiation and propagation steps for ROCOP of $CO_2$ and CHO promoted by **BDI1-D**

| | *anti* | | | *syn* | | |
|---|---|---|---|---|---|---|
| Initiation | **TS1-D$_{R,R}$** | **TS1-D$_{S,S}$** | $\Delta\Delta E^a$ | **TS1-D$_{R,R}$** | **TS1-D$_{S,S}$** | $\Delta\Delta E^a$ |
| $\Delta E_{\text{Strain}}$ | 83.1 | 89.2 | 6.1 | 79.0 | 85.3 | 6.3 |
| $\Delta E_{\text{Strain(Cat+chain)}}$ | 62.6 | 64.1 | 1.5 | 57.9 | 59.6 | 1.6 |
| $\Delta E_{\text{Strain(Mon)}}$ | 20.5 | 25.1 | **4.6** | 21.1 | 25.8 | **4.7** |
| Propagation | **TS1′-D$_{R,R}$** | **TS1′-D$_{S,S}$** | $\Delta\Delta E^a$ | **TS1′-D$_{R,R}$** | **TS1′-D$_{S,S}$** | $\Delta\Delta E^a$ |
| $\Delta E_{\text{Strain}}$ | 78.3 | 85.0 | 6.7 | 72.1 | 73.5 | 1.4 |
| $\Delta E_{\text{Strain(Cat+chain)}}$ | 54.2 | 55.0 | 0.8 | 47.5 | 48.4 | 0.9 |
| $\Delta E_{\text{Strain(Mon)}}$ | 24.1 | 30.0 | **5.9** | 24.6 | 25.1 | **0.5** |

[a] $\Delta\Delta E$ values (kcal $mol^{-1}$) calculated as the difference between each $\Delta E$ term for **TS1-D$_{S,S}$** and **TS1-D$_{R,R}$**.

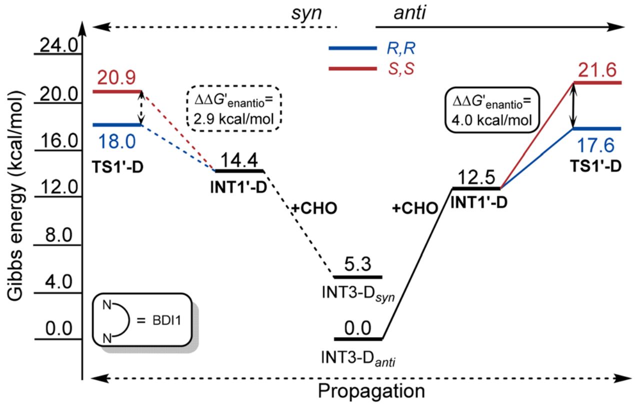

Fig. 5 Gibbs energy profile for the CHO ring-opening on an *R*,*R*-configured growing unit, by **BDI1-D$_{syn}$** (left) and **BDI1-D$_{anti}$** (right). Energies (kcal $mol^{-1}$) are calculated with respect to the more stable **INT3-D$_{anti}$** species. The paths leading to a second *R*,*R*-chain and *S*,*S*-chain formation are reported, respectively, in blue and red.

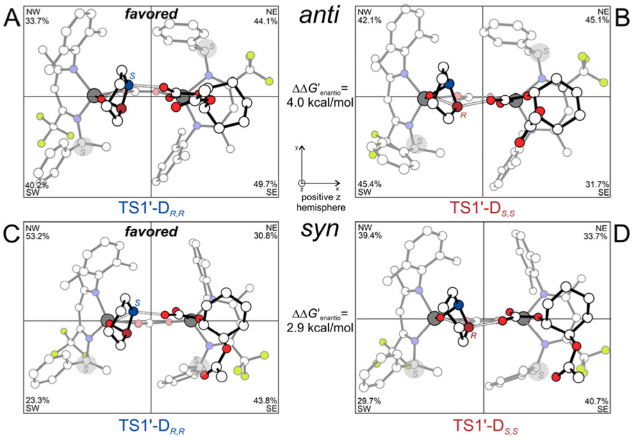

Fig. 6 DFT geometries and %$V_{\text{Bur}}$ (octants) of the RDS of **BDI1-D$_{anti}$** (A and B) and **BDI1-D$_{syn}$** (C and D) species for the propagation of the ROCOP of $CO_2$ and CHO.

The DFT geometries of the relevant TSs along with the %$V_{\text{Bur}}$ steric maps derived from the octant occupancies are reported in Fig. 4. The dimeric active site species shifts the CHO in the more occupied NW and SW octants with respect to **BDI1-M** (Fig. S4†) and this higher occupancy increases the enantioselectivity for both **BDI1-D$_{anti}$** and **BDI1-D$_{syn}$** species.

To complete our understanding of the key factors inferring the ROCOP enantioselectivity, we included also the propagation step, thus simulating the presence of an entire repeating unit (ESI for details, Scheme S1†). Both **BDI1-D$_{anti}$** and **BDI1-D$_{syn}$** were considered, and Fig. 5 reports the minimum energy path of the propagation for **BDI1-D** having an *R*,*R*-configured growing chain. The analogous results for **BDI1-D** species bearing an *S*,*S*-configured growing chain are reported in Fig. S8.† The activation barriers of **BDI1-D$_{syn}$** are comparable to those of the **BDI1-D$_{anti}$** species if calculated with respect to the most stable **INT3-D$_{anti}$**, but sensibly lower if the suitable reference **INT3-D$_{syn}$** is considered. Finally, the enantioselectivity of *both* species is confirmed, with a strong tendency for formation of the *R*,*R*-chain with respect to the *S*,*S*-chain (2.9 and 4.0 kcal $mol^{-1}$, Fig. 5). The ASM analysis on the **BDI1-D** propagating species (Table 2, propagation) confirmed that the $\Delta E_{\text{Strain(Mon)}}$ is the main factor leading to the favored attack on the *S*-configured carbon for **BDI1-D$_{anti}$** (5.9 kcal $mol^{-1}$ higher than **TS1-D$_{R,R}$**, Table 2). For **BDI1-D$_{syn}$**, the picture is less straightforward revealing that the strain energetic variation of both fragments is less dominant. The steric maps analysis (Fig. 6) revealed that, for **BDI1-D$_{anti}$**, the **TS1-D$_{R,R}$** displays lower %$V_{\text{Bur}}$ of the octants around the monomer (NW 33.7% and SW 42.1%) compared to **TS1-D$_{S,S}$**, in which the monomer is again shifted towards the SW octant. For **BDI1-D$_{syn}$**, occupancy of the SW quadrant in **TS1-D$_{S,S}$**, where the monomer is mainly located, is higher than in **TS1-D$_{R,R}$** (29.7% *vs.* 23.3%) but the monomer is partially shifted into the more open NW quadrant.

After careful analysis of the DFT geometries of propagation TSs, we noticed some short distances between hydrogen atoms of the growing chain and fluorine atoms of the $-CF_3$ group of the ligand for the preferred **TS1′-D$_{syn\text{-}R,R}$**. The appearance of a

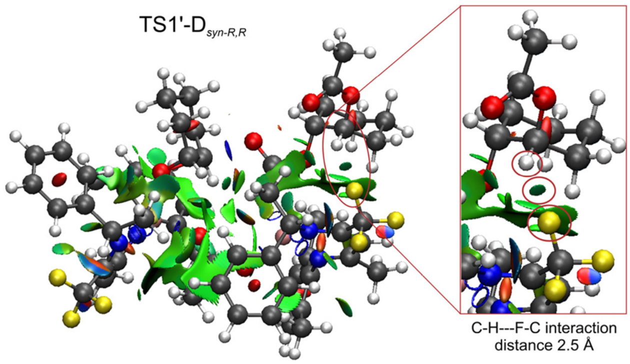

**Fig. 7** Gradient isosurface for the **TS1′-D$_{syn\text{-}R,R}$**. A magnified representation of the interaction of interest is located on the right.

green region of the isosurface between the ligand and the growing chain mentioned above by performing NCI analysis (ESI†), indicates the presence of a weak, attractive interaction (Fig. 7). This interaction, missing in the initiation step, contributes to the stabilization of **TS1′-D$_{syn}$** and highlights the importance of optimizing a complete growing unit in the propagation. As a final check, we also computed the model system by replacing the –$CF_3$ substituents with –$CH_3$ and, accordingly, we calculated a lower enantioselectivity (2.0 *versus* 2.9 kcal mol$^{-1}$; see Fig. S9†).

Noncovalent interactions have previously been proposed in the literature to explain the living olefin polymerization character of Ti-based systems[41] and the heterotactic microstructure of *rac*-LA ROP catalyzed by aluminum systems.[42] However, they have not been reported, to the best of our knowledge, as a factor contributing to the enantioselectivity of the ROCOP. Incidentally, the NCI presence might also explain the ASM results of Table 2 where the minor contribution of the $\Delta E_{\text{Strain}}$ was revealed in particular for the propagation of **BDI1-D$_{syn}$** species.

### *Meso*-desymmetrization amplification moving from $G_1$ to $G_2$ Zn(BDI) species

The last question we want to address in this work is the *meso*-desymmetrization amplification reported for modified **BDI** systems belonging to the $G_2$ generation. It must be recalled that a computational study on the ROCOP promoted by **BDI5** (Scheme 2) has been reported recently by Cramer.[27] This work proposed the participation of the catalyst in both dinuclear (**BDI5-D**) and mononuclear (**BDI5-M**) forms in the reaction, with the former being responsible for CHO ring-opening and the latter for $CO_2$ insertion. The ROCOP promoted by **BDI5-D** was modelled in the initiation reaction by considering the **BDI5-D$_{syn}$** conformation and the enantioselectivity was ascribed to the ligand distortion energies of the two competing TSs involving the epoxide ring-opening. We extended our analysis to **BDI5-D$_{syn}$** simulating not only the initiation (as in the work of Cramer) but also the propagation steps. For the sake of comparison and to be consistent with the previous work, we used the same computational protocol methods reported by Cramer (variation results depending on the computational protocol are reported in Table S1†). Our DFT calculations confirmed the lower enantioselectivity performed by **BDI1-D$_{syn}$** with respect to **BDI5-D$_{syn}$** (Table 3).

**Table 3** Calculated enantioselectivity for the initiation and propagation steps of **BDI1-D$_{syn}$** and **BDI5-D$_{syn}$** at the same level of theory reported in the literature[27]

| | BDI1-D$_{syn}$ | | BDI5-D$_{syn}$ | |
|---|---|---|---|---|
| | Initiation | Propagation | Initiation | Propagation |
| $\Delta\Delta G_{enantio}$ (kcal mol$^{-1}$) | 4.3 | 2.1 | 4.5 | 3.5 |

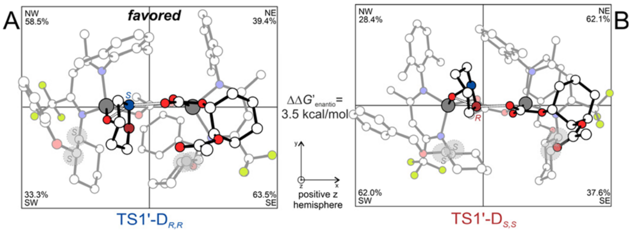

**Fig. 8** DFT geometries and %$V_{\text{Bur}}$ (octants) of the RDS (A and B) for the propagation of the ROCOP of $CO_2$ and CHO at **BDI5-D$_{syn}$**.

The monomer deformation and steric hindrance exerted by the chiral ligand scaffold are crucial for enhancing the enantioselectivity of CHO *meso*-desymmetrization moving from $G_1$ to $G_2$ systems. Specifically, the two RDSs for the propagation at **BDI5-D$_{syn}$** exhibit specular occupancies of the octants located in the north portions *versus* the ones in the south (Fig. 8). This is evidence of strong deformation of **BDI5-D$_{syn}$** occurring in the two TSs especially for **TS1-D$_{S,S}$**, as confirmed also by ASM analysis ($\Delta\Delta E_{\text{Strain(Cat+chain)}}$ = 1.9 kcal mol$^{-1}$, Table S2†), but also of the capability of this system to accommodate the reactants. Indeed, we reasoned that although **BDI5-D$_{syn}$** is sterically more hindered around the monomer, it is also more flexible than **BDI1-D$_{syn}$**. This is evident by looking at the optimized structure and by comparing the %$V_{\text{Bur}}$ of the octants involved (SW and NW) among **BDI1-D$_{syn}$** (Fig. 6C and D) and **BDI5-D$_{syn}$** (Fig. 8A and B).

For **BDI1-D$_{syn}$**, the steric hindrance exerted during the TSs is always localized more in the NW octants than the SW (respectively, 53.2% *vs.* 23.3% for **TS1-D$_{R,R}$**, Fig. 6C, and 39.4% *vs.* 29.2% for **TS1-D$_{S,S}$**, Fig. 6D). For **BDI5-D$_{syn}$**, the steric hindrance "switches" between NW and SW depending on the TS: in **TS1-D$_{R,R}$**, the %$V_{\text{Bur}}$ NW–SW values are 58.5% and 33.3%, respectively (Fig. 8A), whereas in **TS1-D$_{S,S}$** the %$V_{\text{Bur}}$ NW–SW values are 28.4% and 62.0%, respectively (Fig. 8B).

## Conclusions

DFT calculations, combined with ASM analysis and %$V_{\text{Bur}}$ steric maps, provided important insights into the ring-opening copolymerization mechanisms of cyclohexene oxide and carbon dioxide catalyzed by zinc β-diiminate complexes. We claim that the high experimental enantioselectivity reported on the ROCOP of $CO_2$ and CHO by **BDI** complexes is a synergic addition of multiple factors. Chiral zinc monomeric species, although not actively involved in polymerization, already show an intrinsic enantioselective character in the *meso*-desymmetrization ROCOP leading to the *R*,*R*-configured growing chain experimentally traced. This intrinsic property offers a simpler modeling approach for predicting catalyst modifications, being that the modeling of the mononuclear species is far less time consuming.[43] The formation of dimeric species in either the *anti* or *syn* conformation amplifies the CHO ring-opening enantioselectivity and increases the preference for the attack at the *S*-configured carbon leading to the *R*,*R*-growing unit formation. Overall, the enantioselectivity origin of **BDI** catalysts is ascribable to several factors. In both initiation and propagation steps, the monomer deformation, which is a direct consequence of the steric hindrance of the ligand, has been sorted out as the key source of stereoselectivity. Computation of the propagation step with a chiral growing chain revealed the presence of non-covalent interaction between an H atom of the aliphatic bone and fluorine atoms of the ligand contributing to the enantioselectivity. Finally, by a direct comparison between **BDI1-D**, belonging to the first generation, and **BDI5-D**, belonging to the second generation, we reasoned that the origin of the enhanced stereoselectivity for $G_2$ can be attributed to the enhanced flexibility of the catalyst having two chiral centers suitably positioned on the ligand framework. Revealing the effects and their additive rules contributing to the *meso*-desymmetrization catalysis could be a viable route for the synthesis of biodegradable material with tailored properties competing with traditional plastics.[44]

## Author contributions

Y. Rusconi: investigation, conceptualization, writing – review and editing. M. C. D'Alterio: methodology, conceptualization, writing – review and editing. C. De Rosa: writing – review and editing, and supervision. G. W. Coates: writing – review, and supervision. G. Talarico: conceptualization, writing – review and editing, and supervision.

## Data availability

Data for this article, including Tables S1 and S2, Scheme S1, Fig. S1–S9 and cartesian coordinates of the structures discussed are available at **https://doi.org/10.1039/d5gc00523j**.

## Conflicts of interest

There are no conflicts to declare.

## Acknowledgements

This study was carried out within the NEST-Network for Energy Sustainable Transition and received funding from the European Union Next-GenerationEU (Piano Nazionale di Ripresa e Resilineza (PNRR) – Missione 4 Componente 2, Investimento 1.3). This manuscript reflects only the authors' views and opinions, neither the European Union nor the European Commission can be considered responsible for them. Financial support from the project 3A-Italy, MICS–PNRR MUR-M4C2-I 1.3 (PE00000004) is gratefully acknowledged. G. T. thanks the Italian Ministry of University and Research for funding (PRIN 20225RBLK7 (SpeedToBio), CUP E53D23008360006).

## References

1 J. Artz, T. E. Müller, K. Thenert, J. Kleinekorte, R. Meys, A. Sternberg, A. Bardow and W. Leitner, *Chem. Rev.*, 2018, **118**, 434–504.

2 Y. Wang and D. J. Darensbourg, *Coord. Chem. Rev.*, 2018, **372**, 85–100.

3 Z. Guo, Y. Hu, S. Dong, L. Chen, L. Ma, Y. Zhou, L. Wang and J. Wang, *Chem Catal.*, 2022, **2**, 519–530.

4 M. Scharfenberg, J. Hilf and H. Frey, *Adv. Funct. Mater.*, 2018, **28**, 1704302.

5 C. Koning, J. Wildeson, R. Parton, B. Plum, P. Steeman and D. J. Darensbourg, *Polymer*, 2001, **42**, 3995–4004.

6 T. M. McGuire, A. C. Deacy, A. Buchard and C. K. Williams, *J. Am. Chem. Soc.*, 2022, **144**, 18444–18449.

7 F. N. Singer, A. C. Deacy, T. M. McGuire, C. K. Williams and A. Buchard, *Angew. Chem., Int. Ed.*, 2022, **61**, e202201785.

8 M. L. Smith, T. M. McGuire, A. Buchard and C. K. Williams, *ACS Catal.*, 2023, **13**, 15770–15778.

9 Catalysts for enantioselective copolymerization of *meso*-epoxides see: (*a*) Y. Liu, W.-M. Ren, J. Liu and X.-B. Lu, *Angew. Chem., Int. Ed.*, 2013, **52**, 11594–11598; (*b*) B.-H. Ren, Y.-Q. Teng, S.-N. Wang, S. Wang, Y. Liu, W.-M. Ren and X.-B. Lu, *ACS Catal.*, 2022, **12**, 12268–12280.

10 For mechanistic insights see: (*a*) K. Nakano, T. Kamada and K. Nozaki, *Angew. Chem., Int. Ed.*, 2006, **45**, 7274–7277; (*b*) K. Nakano, T. Hiyama and K. Nozaki, *Chem. Commun.*, 2005, 1871–1873; (*c*) K. Nakano, K. Nozaki and T. Hiyama, *J. Am. Chem. Soc.*, 2003, **125**, 5501–5510.

11 J. Huang, J. C. Worch, A. P. Dove and O. Coulembier, *ChemSusChem*, 2020, **13**, 469–487.

12 For experimental works on zinc β-diiminate catalysts see: (*a*) M. Cheng, E. B. Lobkovsky and G. W. Coates, *J. Am. Chem. Soc.*, 1998, **120**, 11018–11019; (*b*) M. Cheng, D. R. Moore, J. J. Reczek, B. M. Chamberlain, E. B. Lobkovsky and G. W. Coates, *J. Am. Chem. Soc.*, 2001, **123**, 8738–8749; (*c*) D. R. Moore, M. Cheng, E. B. Lobkovsky and G. W. Coates, *J. Am. Chem. Soc.*, 2003, **125**, 11911–11924; (*d*) W. C. Ellis, Y. Jung, M. Mulzer, R. Di Girolamo,

E. B. Lobkovsky and G. W. Coates, *Chem. Sci.*, 2014, **5**, 4004–4011.

13 M. I. Childers, J. M. Longo, N. J. Van Zee, A. M. LaPointe and G. W. Coates, *Chem. Rev.*, 2014, **114**, 8129–8152.

14 Á. Enríquez-García and E. P. Kündig, *Chem. Soc. Rev.*, 2012, **41**, 7803–7831.

15 X.-P. Zeng, Z.-Y. Cao, Y.-H. Wang, F. Zhou and J. Zhou, *Chem. Rev.*, 2016, **116**, 7330–7396.

16 T. M. Ovitt and G. W. Coates, *J. Am. Chem. Soc.*, 1999, **121**, 4072–4073.

17 T. M. Ovitt and G. W. Coates, *J. Am. Chem. Soc.*, 2002, **124**, 1316–1326.

18 R. Hador, M. Shuster, V. Venditto and M. Kol, *Angew. Chem., Int. Ed.*, 2022, **61**, e202207652.

19 M. C. D'Alterio, C. De Rosa and G. Talarico, *Chem. Commun.*, 2021, **57**, 1611–1614.

20 M. C. D'Alterio, C. De Rosa and G. Talarico, *ACS Catal.*, 2020, **10**, 2221–2225.

21 Y. Rusconi, M. C. D'Alterio, C. De Rosa, Y. Lu, S. M. Severson, G. W. Coates and G. Talarico, *ACS Catal.*, 2024, **14**, 318–323.

22 G.-W. Yang, R. Xie, Y.-Y. Zhang, C.-K. Xu and G.-P. Wu, *Chem. Rev.*, 2024, **124**, 12305–12380.

23 L. Falivene, Z. Cao, A. Petta, L. Serra, A. Poater, R. Oliva, V. Scarano and L. Cavallo, *Nat. Chem.*, 2019, **11**, 872–879.

24 L. Falivene, L. Cavallo and G. Talarico, *ACS Catal.*, 2015, **5**, 6815–6822.

25 F. M. Bickelhaupt and K. N. Houk, *Angew. Chem., Int. Ed.*, 2017, **56**, 10070–10086.

26 P. Vermeeren, S. C. C. van der Lubbe, C. Fonseca Guerra, F. M. Bickelhaupt and T. A. Hamlin, *Nat. Protoc.*, 2020, **15**, 649–667.

27 H. Shao, Y. Reddi and C. J. Cramer, *ACS Catal.*, 2020, **10**, 8870–8879.

28 M. J. Frisch, G. W. Trucks, H. B. Schlegel, G. E. Scuseria, M. A. Robb, J. R. Cheeseman, G. Scalmani, V. Barone, G. A. Petersson, H. Nakatsuji, X. Li, M. Caricato, A. V. Marenich, J. Bloino, B. G. Janesko, R. Gomperts, B. Mennucci, H. P. Hratchian, J. V. Ortiz, A. F. Izmaylov, J. L. Sonnenberg, D. Williams-Young, F. Ding, F. Lipparini, F. Egidi, J. Goings, B. Peng, A. Petrone, T. Henderson, D. Ranasinghe, V. G. Zakrzewski, J. Gao, N. Rega, G. Zheng, W. Liang, M. Hada, M. Ehara, K. Toyota, R. Fukuda, J. Hasegawa, M. Ishida, T. Nakajima, Y. Honda, O. Kitao, H. Nakai, T. Vreven, K. Throssell, J. A. Montgomery Jr., J. E. Peralta, F. Ogliaro, M. J. Bearpark, J. J. Heyd, E. N. Brothers, K. N. Kudin, V. N. Staroverov, T. A. Keith, R. Kobayashi, J. Normand, K. Raghavachari, A. P. Rendell, J. C. Burant, S. S. Iyengar, J. Tomasi, M. Cossi, J. M. Millam, M. Klene, C. Adamo, R. Cammi, J. W. Ochterski, R. L. Martin, K. Morokuma, O. Farkas, J. B. Foresman and D. J. Fox, *Gaussian 16 Rev. C.01*, Wallingford, CT, 2016.

29 (*a*) A. D. Becke, *J. Chem. Phys.*, 1993, **98**, 5648; (*b*) C. Lee, W. Yang and R. G. Parr, *Phys. Rev. B: Condens. Matter Mater. Phys.*, 1988, **37**, 785–789.

30 A. Schäfer, H. Horn and R. Ahlrichs, *J. Chem. Phys.*, 1992, **97**, 2571–2577.

31 V. Barone and M. Cossi, *J. Phys. Chem. A*, 1998, **102**, 1995–2001.

32 S. Grimme, *J. Comput. Chem.*, 2004, **12**, 1463–1473.

33 S. F. Boys and F. Bernardi, *Mol. Phys.*, 1970, **19**, 553–566.

34 J.-D. Chai and M. Head-Gordon, *Phys. Chem. Chem. Phys.*, 2008, **10**, 6615–6620.

35 L. Falivene, V. Barone and G. Talarico, *Mol. Catal.*, 2018, **452**, 138–144.

36 J. Contreras-García, E. R. Johnson, S. Keinan, R. Chaudret, J.-P. Piquemal, D. N. Beratan and W. Yang, *J. Chem. Theory Comput.*, 2011, **7**, 625–632.

37 For the application of ASM analysis on the α-olefin polymerization transition metal catalyzed see: (*a*) E. Romano, V. Barone, P. H. M. Budzelaar, C. De Rosa and G. Talarico, *Chem. – Asian J.*, 2024, **19**, e202400155; (*b*) A. Cicolella, E. Romano, V. Barone, C. De Rosa and G. Talarico, *Organometallics*, 2022, **41**, 3872–3883; (*c*) E. Romano, P. H. M. Budzelaar, C. De Rosa and G. Talarico, *J. Phys. Chem. A*, 2022, **126**, 6203–6209; (*d*) F. Núñez-Zarur and A. Comas-Vives, *J. Phys. Chem. C*, 2022, **126**, 296–308; (*e*) Y. Zhao, X. Xu, Y. Wang, T. Liu, H. Li, Y. Zhang, L. Wang, X. Wang, S. Zhao and Y. Luo, *RSC Adv.*, 2022, **12**, 21111–21121.

38 For the application of ASM analysis on the ROP of LA see: (*a*) M. C. D'Alterio, S. Moccia, Y. Rusconi, C. De Rosa and G. Talarico, *Catal. Sci. Technol.*, 2024, **14**, 5624–5633; (*b*) S. Moccia, M. C. D'Alterio, E. Romano, C. De Rosa and G. Talarico, *Macromol. Rapid Commun.*, 2025, **46**, 2400733.

39 J. González-Fabra, F. Castro-Gómez, A. W. Kleij and C. Bo, *ChemSusChem*, 2017, **10**, 1233–1240.

40 I. D'Auria, M. C. D'Alterio, G. Talarico and C. Pellecchia, *Macromolecules*, 2018, **51**, 9871–9877.

41 For selected reports on the noncovalent interaction on olefin polymerization see: (*a*) M. Mitani, T. Nakano and T. Fujita, *Chem. – Eur. J.*, 2003, **9**, 2396–2403; (*b*) K. P. Bryliakov, E. P. Talsi, H. M. Möller, M. C. Baier and S. Mecking, *Organometallics*, 2010, **29**, 4428–4430; (*c*) M. P. Weberski, C. Chen, M. Delferro, C. Zuccaccia, A. Macchioni and T. J. Marks, *Organometallics*, 2012, **31**, 3773–3789; (*d*) C.-C. Liu and M. C. W. Chan, *Acc. Chem. Res.*, 2015, **48**, 1580–1590; (*e*) G. Talarico and P. H. M. Budzelaar, *Organometallics*, 2016, **35**, 47–54; (*f*) L. Falivene, L. Cavallo and G. Talarico, *Mol. Catal.*, 2020, **494**, 111118; (*g*) Y. Cornaton and J.-P. Djukic, *Acc. Chem. Res.*, 2021, **54**, 3828–3840.

42 S. Gesslbauer, R. Savela, Y. Chen, A. J. P. White and C. Romain, *ACS Catal.*, 2019, **9**, 7912–7920.

43 Z. Cao, L. Falivene, A. Poater, B. Maity, Z. Zhang, G. Takasao, S. B. Sayed, A. Petta, G. Talarico, R. Oliva and L. Cavallo, *Cell Rep. Phys. Sci.*, 2025, **6**, 102348.

44 J. W. Han, F. Hollmann, R. Luque, I. K. Song, G. Talarico, T. Tatsumi and N. Yan, *Mol. Catal.*, 2022, **522**, 112233.